Gravitational Lensing with Halo Substructure

Jakob Jönsson

April 10, 2002

Filosofie Magisterexamen

Stockholm University
Department of Physics

Acknowledgements

I would like to thank my supervisor Lars Bergström for his help and encouraging support.

Abstract

Smooth density profiles of galaxy halos has succesfully been used to model gravitational lensing systems. There are indications that dark matter halos contain substructure. In this paper the effects of substructure in a smooth host halo are explored by numerical simulations. The basic theory of gravitational lensing is reviewed and a model for compound gravitational lensing is presented. The effects of different forms and distributions of substructure are investigated. The results were found to be in agreement with previous simulations except for those for the largest subhalos. An example of secondary images caused by the presence of substructure is also presented. Furtermore the reliability of the method and the sensitivity to the simulation parameters are discussed.

Contents

1 Introduction **4**

2 Theory **4**
- 2.1 General gravitational lenses . . . 5
  - 2.1.1 Derivation of the lens equation . . . 5
  - 2.1.2 The scaled lens equation . . . 6
  - 2.1.3 The deflection potential . . . 7
  - 2.1.4 The magnification factor . . . 7
  - 2.1.5 The angular diameter distance . . . 8
- 2.2 Axially symmetric lenses . . . 8
  - 2.2.1 The singular isothermal sphere . . . 9
- 2.3 The substructure model . . . 10
  - 2.3.1 Mass and radius of the substructure . . . 10
  - 2.3.2 The deflection angle for a truncated SIS . . . 10
  - 2.3.3 The deflection angle for a pointlike object with mass $m(\sigma, R)$ 12

3 Documentation of the simulation **13**
- 3.1 The lensing equation used in the simulation . . . 13
- 3.2 The grid setup . . . 15
- 3.3 The substructure setup . . . 15
  - 3.3.1 The probability distribution . . . 15
  - 3.3.2 The generation of random numbers . . . 16
  - 3.3.3 The total mass of the substructure . . . 16
- 3.4 The deflection angles caused by the substructure . . . 17
  - 3.4.1 Truncated SIS treated as point masses . . . 17
  - 3.4.2 Approximation of the delta–function . . . 17
  - 3.4.3 Refined calculation of $\vec{\alpha}_{sub}(\vec{x})$ . . . 19
  - 3.4.4 The outcome of the lensing equation . . . 19

4 Results of the simulations **20**
- 4.1 Lensing parameters . . . 20
- 4.2 Different distributions of substructure . . . 20
- 4.3 Image splitting . . . 21
- 4.4 Comparison with Metcalf and Madau . . . 22
- 4.5 Reliability of the method . . . 24
  - 4.5.1 Image resolution . . . 25
  - 4.5.2 The size of the grid . . . 27
  - 4.5.3 Statistics . . . 27

5 Conclusions **28**

1 Introduction

The sky is full of bright stars, but these luminous objects are supposed to make up only a small part of the universe. Most of the universe consists of dark matter. Dark matter does not emit any radiation and is therefore not visible. The luminous matter in galaxies is supposed to be surrounded by a halo of dark matter. The nature of dark matter halos will be of interest in this paper.

Even though dark matter does not radiate it can still be detected. Dark matter reveals itself by the gravitational force it exerts. One of the consequences of Einstein's theory of general relativity is that light is bent by mass. The gravitational field of a deflecting mass, called the gravitational lens, can focus the light of a source and give rise to multiple images of it. These images can be magnified or demagnified relative to the source. This is called gravitational lensing. Gravitational lensing is a powerful tool for testing different models of dark matter.

Smooth density profiles have been successfully used to model gravitational lenses. There are however indications that the galactic halos are more complex than these models. For some gravitational lensing systems the smooth models have been able to predict the image positions, but failed to explain the observed flux ratios of the images [1]. Substructure within the halos might be a solution to this problem.

Another important reason to study the effects of halo substructure is the so called "small scale crisis" [2]. According to numerical simulations, based on the cold dark matter (CDM) scenario for structure formation, galaxies should resemble scaled down versions of galaxy clusters. The simulations predict the existence of several hundred subclumps within the Milky Way halo, but only a dozen have been observed.

In this paper gravitational lensing with halo substructure will be investigated by numerical simulations. Compound gravitational lensing has recently been studied by Metcalf and Madau [3]. They used a smooth host halo with a few percent of the mass contained in subhalos. They claimed that this substructure affect the magnification ratios appreciably while the image positions are almost the same. One of the purposes of this paper is to try to reproduce the results of Metcalf and Madau.

The outline of the paper is the following. First the basic framework of gravitational lensing and models for the host halo and substructure is presented. After that follows a description of a method to do numerical simulations of compound gravitational lensing. Finally the results of the simulations are presented and discussed.

2 Theory

In this section the theory needed to model a compound gravitational lensing system is presented. The theory is taken from the references [4] and [5].

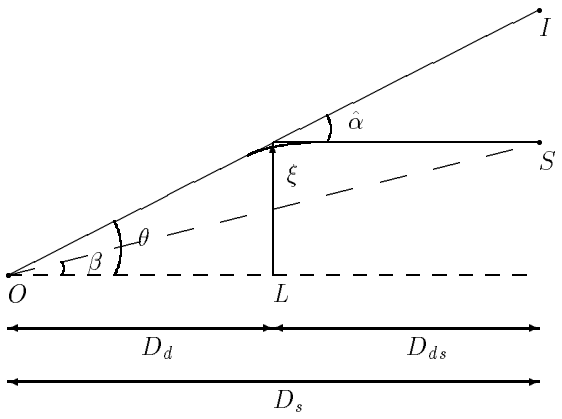

Figure 1: A general gravitational lensing system. The center of the lens is at L. The line trough L and the observer O serve as a reference line and is called the "optical axis". Relative to the optical axis, the source S has an undisturbed angular position β. A light ray SO from the source is deflected by an angle $\hat{\alpha}$, so that the image I is observed at the position θ. The distances from the observer to the lens and the source are D_d and D_s respectively. D_{ds} denotes the distance from the lens to the source.

2.1 General gravitational lenses

2.1.1 Derivation of the lens equation

In figure 1 a general lensing system is depicted. The system consists of a source, a gravitational lens and an observer. The source S and the lens L both lie on spheres centered on the observer O. The radii of the source and lens spheres are D_s and D_d respectively. The deflection angle of the light is in all cases of astrophysical interest so small, that the spheres can be approximated with their tangent planes. The planes corresponding to source and lens spheres are called source plane and lens plane respectively. From the geometry of figure 1, a relation between the angular position $\vec{\beta}$ of the unlensed source and the angular position $\vec{\theta} = \vec{\xi}/D_d$ of the image can be derived:

$$\vec{\beta} = \vec{\theta} - \frac{D_{ds}}{D_s}\hat{\vec{\alpha}} \tag{1}$$

where $\hat{\vec{\alpha}}$ is the deflection angle of the light ray. This is the so–called lens equation. It can be rewritten in terms of the physical vectors $\vec{\eta} = D_s\vec{\beta}$ and $\vec{\xi}$ in the source and lens plane respectively:

$$\vec{\eta} = \frac{D_s}{D_d}\vec{\xi} - D_{ds}\hat{\vec{\alpha}}(\vec{\xi}) \tag{2}$$

The thickness of the lens is typically much smaller than the distances D_s and D_d. The lens can therefore be approximated by a thin screen in the lens plane. The mass distribution $\rho(\vec{\xi}, z)$ of the lens can then be projected along the line–of–sight (i.e. the z–axis) and be replaced by a mass sheet orthogonal to the line of sight. This mass sheet is characterized by its surface mass density:

$$\Sigma(\vec{\xi}) = \int_{-\infty}^{\infty} \rho(\vec{\xi}, z)\, dz \tag{3}$$

The deflection angle caused by a point with mass m located at $\vec{\xi}'$ is:

$$\hat{\vec{\alpha}}(\vec{\xi}) = \frac{4Gm}{c^2} \frac{\vec{\xi} - \vec{\xi}'}{|\vec{\xi} - \vec{\xi}'|^2} \tag{4}$$

where G is Newtons gravitational constant and c is the speed of light. For an extended matter distribution the deflection angle is given by the sum of the deflections due to all mass elements in the lens plane:

$$\hat{\vec{\alpha}}(\vec{\xi}) = \frac{4G}{c^2} \int_{\mathcal{R}^2} d^2\xi' \Sigma(\vec{\xi}') \frac{\vec{\xi} - \vec{\xi}'}{|\vec{\xi} - \vec{\xi}'|^2} \tag{5}$$

2.1.2 The scaled lens equation

It is useful to rewrite the lens equation (2) and the surface mass density (3) in dimensionless form. To do this first one defines a length scale ξ_0 in the lens plane and a corresponding length scale $\eta_0 = \xi_0 D_s / D_d$ in the source plane. Then one defines the dimensionless vectors:

$$\vec{x} = \frac{\vec{\xi}}{\xi_0} \quad ; \quad \vec{y} = \frac{\vec{\eta}}{\eta_0} \tag{6}$$

as well as the dimensionless surface mass density:

$$\kappa(\vec{x}) = \frac{\Sigma(\xi_0 \vec{x})}{\Sigma_{cr}} \tag{7}$$

where the critical surface density Σ_{cr} is defined as:

$$\Sigma_{cr} = \frac{c^2 D_s}{4\pi G D_d D_{ds}} \tag{8}$$

The lens equation (2) can then, with the help of equations (6) and (7), be written in the dimesionless form:

$$\vec{y} = \vec{x} - \vec{\alpha}(\vec{x}) \tag{9}$$

where:

$$\vec{\alpha}(\vec{x}) = \frac{1}{\pi} \int_{\mathcal{R}^2} d^2x' \kappa(\vec{x}') \frac{\vec{x} - \vec{x}'}{|\vec{x} - \vec{x}'|^2} = \frac{D_d D_{ds}}{\xi_0 D_s} \hat{\vec{\alpha}}(\xi_0 \vec{x}) \tag{10}$$

2.1.3 The deflection potential

The identity $\nabla \ln|\vec{x}| = \frac{\vec{x}}{|\vec{x}|^2}$ shows that the deflection angle (10) can be written as the gradient of a potential $\psi(\vec{x})$:

$$\vec{\alpha}(\vec{x}) = \nabla\psi(\vec{x}) \tag{11}$$

where:

$$\psi(\vec{x}) = \frac{1}{\pi}\int_{\mathcal{R}^2} d^2x'\kappa(\vec{x}')\ln|\vec{x}-\vec{x}'| \tag{12}$$

The relation (12) giving ψ in terms of κ can be inverted via the identity $\nabla^2\ln(\vec{x}) = 2\pi\delta^2(\vec{x})$ to give Poisson's equation:

$$\nabla^2\psi(\vec{x}) = 2\kappa(\vec{x}) \tag{13}$$

2.1.4 The magnification factor

Gravitational light deflection can magnify or demagnify the images of a source. The differential deflection across a light bundle affects the properties of the images. Since surface brightness is conserved, the flux of an image is determined by this area distortion. Consider an infinitesimal source with surface brightness I_ν, where ν is the observed frequency. In the absence of gravitational light deflection this source subtends a solid angle $d\omega^*$ on the sky. The monocromatic flux from this source is:

$$S^*_\nu = I_\nu d\omega^* \tag{14}$$

If the light bundle undergoes deflection the solid angle of the image $d\omega$ will differ from $d\omega^*$. Since the light bending affects neither ν nor I_ν the observed flux from the image is:

$$S_\nu = I_\nu d\omega \tag{15}$$

the light deflection leads to a change of the observed flux by a factor:

$$|\mu| = \frac{S_\nu}{S^*_\nu} = \frac{d\omega}{d\omega^*} \tag{16}$$

$|\mu|$ is called the magnification factor. The solid angles can be expressed as $d\omega = d^2\xi/D_d^2$ and $d\omega^* = d^2\eta/D_s^2$. The magnification factor can then be rewritten as:

$$|\mu| = \frac{d^2\xi}{d^2\eta}\left(\frac{D_s}{D_d}\right)^2 \tag{17}$$

If the scaled vectors (6) are used equation (17) becomes:

$$|\mu| = \frac{d^2x}{d^2y} \tag{18}$$

It is thus seen that the magnifiaction factor $|\mu|$ can be obtained from the Jacobian determinant, which describes the area distortion of the lens mapping (9). If the Jacobian matrix for the lens mappig is defined as:

$$A(\vec{x}) = \frac{\partial \vec{y}}{\partial \vec{x}} \tag{19}$$

then the magnification factor can consequently be defined as:

$$\mu(\vec{x}) = \frac{1}{\det A(\vec{x})} \tag{20}$$

Equation (19) and equation (11) imply that:

$$A_{ij} = \delta_{ij} - \psi_{ij} \tag{21}$$

where the partial derivatives of the scalar function ψ with respect to x_i are denoted by the subscripts i.

2.1.5 The angular diameter distance

Distances in the universe are not directly observable. The distances used in the formulas depend on the choice of cosmology. In this paper an Einstein–de Sitter universe, corresponding to $\Omega = 1$, is assumed. The angular diameter distance D can be written as:

$$D = \frac{c}{H_0} r(z) \tag{22}$$

where H_0 is the Hubble constant and $r(z)$ is the "dimensionless Dyer–Roeder distance". The distance $r(z)$ dependens on the observable redshift z. The explicit solution to the Dyer–Roeder equation for an Einstein–de Sitter universe is:

$$r(z) = \frac{(1+z)^{\beta} - (1+z)^{-\beta}}{2\beta(1+z)^{5/4}} \tag{23}$$

where $\beta = \sqrt{25 - 24\tilde{\alpha}}$ depends of the clumpiness parameter $\tilde{\alpha}$. Throughout this paper the background cosmology is supposed to be smooth, corresponding to $\tilde{\alpha} = 1$.

2.2 Axially symmetric lenses

In the case of axisymmetric lenses, $\Sigma(\vec{\xi}) = \Sigma(|\vec{\xi}|)$, the formulas above become particularly simple. The notation $x = |\vec{x}|$ is used below. The deflection angle (10) for an axisymmetric lens is:

$$\vec{\alpha}(\vec{x}) = \frac{m(x)}{x}\hat{x} \tag{24}$$

where:

$$m(x) = \int_0^x x' dx' \kappa(x') \tag{25}$$

The deflection potential (12) for an axially symmetric mass distribution is:

$$\psi(x) = 2 \int_0^x x' dx' \kappa(x') \ln\left(\frac{x}{x'}\right) \tag{26}$$

2.2.1 The singular isothermal sphere

A mass distribution often used to model gravitational lenses is the Singular Isothermal Sphere (SIS). The density profile of the SIS is:

$$\rho(r) = \frac{\sigma^2}{2\pi G r^2} \tag{27}$$

where σ is the line–of–sight velocity dispersion and r is the distance from the core. The corresponding surface mass density is obtained by equation (3):

$$\Sigma(\vec{\xi}) = \frac{\sigma^2}{2\pi G} \int_{-\infty}^{\infty} \frac{1}{\xi^2 + z^2} dz = \frac{\sigma^2}{2\pi G} \left[\frac{1}{\xi} \arctan \frac{z}{\xi}\right]_{-\infty}^{\infty} = \frac{\sigma^2}{2G\xi} \tag{28}$$

where $\xi = |\vec{\xi}|$. The natural length scale for a SIS is:

$$\xi_0 = 4\pi \left(\frac{\sigma}{c}\right)^2 \frac{D_d D_{ds}}{D_s} \tag{29}$$

With this length scale the dimensionless surface mass density, defined by equation (7), becomes:

$$\kappa(x) = \frac{1}{2x} \tag{30}$$

The deflection angle (24) for a SIS is $\vec{\alpha}(\vec{x}) = \frac{\vec{x}}{x}$. The lens equation is thus:

$$\vec{y} = \vec{x} - \frac{\vec{x}}{x} \tag{31}$$

The deflection potential (26) for a SIS is $\psi(\vec{x}) = x$. Together with equation (21) this give the Jacobian matrix:

$$A(\vec{x}) = \begin{pmatrix} 1 - \frac{x_2^2}{x^3} & \frac{x_1 x_2}{x^3} \\ \frac{x_1 x_2}{x^3} & 1 - \frac{x_1^2}{x^3} \end{pmatrix} \tag{32}$$

This implies that $\det A(\vec{x}) = 1 - \frac{1}{x}$ which in turn implies that the magnification factor is:

$$\mu = \frac{x}{x-1} \tag{33}$$

2.3 The substructure model

2.3.1 Mass and radius of the substructure

Metcalf and Madau model a compound lens as a smooth host halo with subhalos. The substructure is only realized in a simulation region where it will make up a fraction f_Σ of the mass of the host halo. The host halo is modeled as a SIS and the subhalos are modeled as truncated SIS. The masses and radii of the subclumps, as given in [3], are:

$$m(\sigma, R) = \frac{2R\sigma^3}{\sqrt{3}G\sigma_{halo}} \quad \text{and} \quad r(\sigma, R) = \frac{R\sigma}{\sqrt{3}\sigma_{halo}} \tag{34}$$

where R is the distance from the center of the host halo and σ_{halo} is the velocity dispersion of the host halo. σ is the velocity dispersion of the subclump. The truncation radius and the mass of the sphere are related to each other. The truncation radius $r(\sigma, R)$ is given by:

$$m(\sigma, R) = \int_{\mathcal{R}^3} \rho(r) r^2 dr d\Omega = \frac{2\sigma^2}{G} \int_0^{r(\sigma,R)} dr = \frac{2\sigma^2}{G} r(\sigma, R) \tag{35}$$

The properties of the subhalos can therefore equally well be described by $m(\sigma, R)$ or $r(\sigma, R)$.

2.3.2 The deflection angle for a truncated SIS

The truncated singular isothermal sphere has the following mass density expressed in spherical coordinates (r, θ, ϕ):

$$\rho(r) = \begin{cases} \frac{\sigma^2}{2\pi G}\frac{1}{r^2} & \text{if } r < r(\sigma, R) \\ 0 & \text{if } r > r(\sigma, R) \end{cases} \tag{36}$$

When projecting upon the line–of–sight, cylindrical coordinates (ξ, ϕ, z) is a better choice:

$$\rho(\xi, z) = \begin{cases} \frac{\sigma^2}{2\pi G}\frac{1}{\xi^2+z^2} & \text{if } \xi^2 + z^2 < r^2(\sigma, R) \\ 0 & \text{if } \xi^2 + z^2 > r^2(\sigma, R) \end{cases} \tag{37}$$

The surface mass density, given by equation (3), is:

$$\Sigma(\xi) = \int_{-\sqrt{r^2(\sigma,R)-\xi^2}}^{\sqrt{r^2(\sigma,R)-\xi^2}} \frac{\sigma^2}{2\pi G} \frac{1}{\xi^2 + z^2} dz \tag{38}$$

The integrand of (38) is even, which can be used to simplify the integral. If the coordinates are changed to $y = z/\xi$ the integral can be simplified even more:

$$\Sigma(\xi) = \frac{\sigma^2}{\pi G \xi} \int_0^{\sqrt{\left(\frac{r(\sigma,R)}{\xi}\right)^2 - 1}} \frac{1}{1+y^2} dy = \frac{\sigma^2}{\pi G \xi} \arctan\left(\sqrt{\left(\frac{r(\sigma, R)}{\xi}\right)^2 - 1}\right) \tag{39}$$

The dimensionless surface mass density can be calculated with the use of equation (7) and the length scale (29):

$$\kappa(x) = \frac{1}{\pi x} \arctan\left(\sqrt{\left(\frac{r(\sigma,R)}{\xi_0 x}\right)^2 - 1}\right) \tag{40}$$

where $x = |\vec{x}|$ as before. The truncated SIS is axially symmetric so the deflection angle can be calculated by using equation (24).

$$m(x) = \frac{2}{\pi}\int_0^x \arctan\left(\sqrt{\left(\frac{r(\sigma,R)}{\xi_0 x'}\right)^2 - 1}\right) dx' \tag{41}$$

If the variable $s = \frac{r(\sigma,R)}{\xi_0 x'}$ is used, then the integral (41) adopts a simpler form:

$$m(s) = \frac{2}{\pi}\frac{r(\sigma,R)}{\xi_0}\int_{\frac{r(\sigma,R)}{\xi_0 x}}^{\infty} \frac{1}{s^2}\arctan\left(\frac{\sqrt{s^2-1}}{s}\right) ds$$

$$\Leftrightarrow m(s) = \frac{2}{\pi}\frac{r(\sigma,R)}{\xi_0}\left[\frac{\sqrt{s^2-1}}{s} - \frac{\arctan(\sqrt{s^2-1})}{s}\right]_{\frac{r(\sigma,R)}{\xi_0 x}}^{\infty} \tag{42}$$

Since $\lim_{s\to\infty}\left(\frac{\sqrt{s^2-1}}{s} - \frac{\arctan(\sqrt{s^2-1})}{s}\right) = 1$, the upper limit in (42) gives $2r(\sigma,R)/\pi\xi_0$. The lower limit gives rise to two different expressions depending on whether $x\xi_0$ is larger or smaller than the radius of the subclump $r(\sigma,R)$. Since all of the surface matter density of the subclumps is contained inside a disc with radius $r(\sigma,R)$, the integrand vanishes for $x\xi_0 > r(\sigma,R)$. When $r(\sigma,R)/x\xi_0 < 1$ equation (42) therefore implies:

$$m(x) = \frac{2}{\pi}\frac{r(\sigma,R)}{\xi_0} \tag{43}$$

When $r(\sigma,R)/x\xi_0 > 1$ equation (42) instead gives:

$$m(x) = \frac{2}{\pi}x\left(\frac{r(\sigma,R)}{\xi_0 x} - \sqrt{\left(\frac{r(\sigma,R)}{\xi_0 x}\right)^2 - 1} + \arctan\left(\sqrt{\left(\frac{r(\sigma,R)}{\xi_0 x}\right)^2 - 1}\right)\right) \tag{44}$$

In the simulations it is necessary to use one length scale for truncated SIS with different velocity dispersion. This length scale is chosen to be the one corresponding to the largest subhalo, $\xi_0(\sigma_{max})$. $\xi_0(\sigma)$ is the natural length scale (29) for the SIS. The deflection angle caused by smaller subhalos is therefore multiplied with a factor $\xi_0(\sigma)/\xi_0(\sigma_{max}) = \sigma^2/\sigma_{max}^2$. It is also convenient to introduce $a = r(\sigma,R)/\xi_0(\sigma_{max})x$ where x is defined by equation (6) for $\xi_0(\sigma_{max})$. If the distance x is meassured in units of $\xi_0(\sigma_{max})$, then $r(\sigma,R)/\xi_0(\sigma)x' =$

$r(\sigma, R)/\xi_0(\sigma_{max})x$, where the primed x denotes the distance meassured in terms of $\xi_0(\sigma)$.

Finally the deflection angle (24) caused by a truncated SIS is given by:

$$\vec{\alpha}(\vec{x}) = \hat{x}\frac{2}{\pi}\left(\frac{\sigma}{\sigma_{max}}\right)^2 \begin{cases} a - \sqrt{a^2-1} + \arctan(\sqrt{a^2-1}) & \text{if } a > 1 \\ a & \text{if } a > 1 \end{cases} \tag{45}$$

2.3.3 The deflection angle for a pointlike object with mass $m(\sigma, R)$

The deflection angles for a truncated SIS and a point mass are identical when $a < 1$. This will be shown below. The surface mass density of a point with mass M is given by $\Sigma(\vec{\xi}) = M\delta^2(\vec{\xi})$. According to the definition (7) the dimensionless surface density for a point mass is:

$$\kappa(\vec{x}) = \frac{M\delta^2(\xi_0\vec{x})}{\Sigma_{cr}} \tag{46}$$

The identities $\delta^2(\vec{x}) = \delta(x_1)\delta(x_2)$ and $\delta(ax) = \frac{1}{|a|}\delta(x)$ can be used to rewrite the two–dimensional delta–function as $\delta^2(\xi_0\vec{x}) = \delta^2(\vec{x})/\xi_0^2$. If $M = m(\sigma, R) = \frac{2\sigma^2}{G}r(\sigma, R)$ and the definition (8) of Σ_{cr} is inserted into equation (46), the following equation is obtained:

$$\kappa(\vec{x}) = \frac{2r(\sigma, R)}{\xi_0^2}\frac{4\pi\sigma^2 D_d D_{ds}}{c^2 D_s}\delta^2(\vec{x}) \tag{47}$$

In this equation one can identify the length scale (29) for a SIS. This length scale is related to the subclump mass. If $\xi_0(\sigma_{max})$ is chosen as the length scale for the distances, then the dimensionless surface density is:

$$\kappa(\vec{x}) = \frac{2r(\sigma, R)\xi_0(\sigma)}{\xi_0^2(\sigma_{max})}\delta^2(\vec{x}) = \left(\frac{\sigma}{\sigma_{max}}\right)^2\frac{2r(\sigma, R)}{\xi_0(\sigma_{max})}\delta^2(\vec{x}) \tag{48}$$

The deflection angle can then be calculated by equation (10):

$$\vec{\alpha}(\vec{x}) = \frac{2}{\pi}\left(\frac{\sigma}{\sigma_{max}}\right)^2\frac{r(\sigma, R)}{\xi_0(\sigma_{max})}\int_{\mathcal{R}^2} d^2x'\delta^2(\vec{x}')\frac{\vec{x}-\vec{x}'}{|\vec{x}-\vec{x}'|^2}$$

$$\Leftrightarrow \vec{\alpha}(\vec{x}) = \frac{2}{\pi}\left(\frac{\sigma}{\sigma_{max}}\right)^2\frac{r(\sigma, R)}{\xi_0(\sigma_{max})}\frac{\vec{x}}{|\vec{x}|^2} = \frac{2}{\pi}\left(\frac{\sigma}{\sigma_{max}}\right)^2 a\hat{x} \tag{49}$$

This is the same expression as for the truncated SIS with $a < 1$. Thus, outside a truncated SIS the deflection angle is the same as for a pointlike object with the same mass. This equality will later be used in the simulation. The corresponding deflection potential, given by equation (12), is:

$$\psi(\vec{x}) = \frac{2}{\pi}\left(\frac{\sigma}{\sigma_{max}}\right)^2\frac{r(\sigma, R)}{\xi_0(\sigma_{max})}\int_{\mathcal{R}^2} d^2x'\delta^2(\vec{x}')\ln|\vec{x}-\vec{x}'|$$

$$\Leftrightarrow \psi(\vec{x}) = \frac{2}{\pi}\left(\frac{\sigma}{\sigma_{max}}\right)^2 \frac{r(\sigma,R)}{\xi_0(\sigma_{max})} \ln|\vec{x}| \tag{50}$$

3 Documentation of the simulation

The method used for simulating compound gravitational lensing is essentially the same as the one Metcalf and Madau used in their paper.

First, models are chosen for the host halo and the substructure. Second, a random configuration of substructure is created. Then the deflection angle caused by the substructure is calculated on a grid in the lens plane. Thereafter the lens equation is used to decide which gridpoints in the lens plane correspond to a given source. This information is then used to calculate the magnification of each image of the source.

A singular isothermal sphere is used to model the host halo. The subhalos are modelled as truncated singular isothermal spheres. A useful property of the truncated SIS is that outside the radius of the sphere the deflection angle is the same as for a point mass. The deflection angles caused by the substructure can in principle be calculated by superposition of the deflection angles caused by each subclump. Since the number of subhalos and the number of gridpoints are both large, such a calculation would be quite time–consuming. A faster way to calculate the deflection angles is therefore desired. Outside the radius of the subclump the contribution to the deflection angle can be treated as if it originated from a point mass. The calculation of the deflection angles caused by the substructure is therefore carried out in two steps. First all subclumps are treated as point masses. At a second stage a refined calculation is carried out in the neighbourhood of each clump.

The simulation was written in the programming language FORTRAN77 [7].

3.1 The lensing equation used in the simulation

The simulation region covers only a small part of the area of the host halo in the lens plane. This makes it necessary to treat the contributions from the halo outside the simulation region in some way. The method used by Metcalf and Madau is presented below. The fraction of the host halo that consists of substructure is denoted f_Σ. If this fraction of substructure is considered only in the simulation region, then the surface density of the host halo can be written:

$$\kappa_{halo}(\vec{x}') = \begin{cases} \kappa_{smooth}(\vec{x}') & \text{outside simulation region} \\ [1 - f_\Sigma(\vec{x}_0)]\kappa_{smooth}(\vec{x}') & \text{inside simulation region} \end{cases} \tag{51}$$

where $\vec{x}_0$ is the center of the simulation region and f_Σ is supposed not to change within the simulation region. In addition the host halo is supposed to be smooth. According to the principle of linear superposition, the small deflection angles add. The lensing equation inside the simulation region can thus be written:

$$\vec{y}' = \vec{x}' - \vec{\alpha}'_{halo}(\vec{x}') - \vec{\alpha}'_{sub}(\vec{x}') \tag{52}$$

It is convienient to let the center of the simulation region and the image of the smooth macro lens coincide. In the absence of substructure the image appears at $\vec{x}_0$ and the lensing equation is:

$$\vec{y}_0 = \vec{x}_0 - \vec{\alpha}_{smooth}(\vec{x}_0) \tag{53}$$

Inserting equation (53) into equation (52) and changing coordinates to $\vec{x} = \vec{x}' - \vec{x}_0$ and $\vec{y} = \vec{y}' - \vec{y}_0$ will give:

$$\vec{y} = \vec{x} - \vec{\alpha}_{halo}(\vec{x} + \vec{x}_0) + \vec{\alpha}_{smooth}(\vec{x}_0) - \vec{\alpha}_{sub}(\vec{x} + \vec{x}_0) \tag{54}$$

It is desirable to have an expression whitout $\vec{\alpha}_{halo}(\vec{x})$. If the surface density inside the simulation region can be approximated as constant, then the following approximation can be made:

$$\kappa_{smooth}(\vec{x}') - \kappa_{halo}(\vec{x}') = f_\Sigma \kappa_{smooth}(\vec{x}') \approx f_\Sigma \kappa_{smooth}(\vec{x}_0) \tag{55}$$

After adding and subtracting $\alpha_{smooth}(\vec{x} + \vec{x}_0)$ to equation (54) and rearranging the terms, the following equation is obtained:

$$\vec{y} = \vec{x} + \vec{\alpha}_{smooth}(\vec{x} + \vec{x}_0) - \vec{\alpha}_{halo}(\vec{x} + \vec{x}_0) +$$

$$+ \vec{\alpha}_{smooth}(\vec{x}_0) - \vec{\alpha}_{smooth}(\vec{x} + \vec{x}_0) - \vec{\alpha}_{sub}(\vec{x} + \vec{x}_0) \tag{56}$$

A relation between the surface density and the deflection angle can be obtained by integration of Poisson's equation (13):

$$\vec{\alpha}_{smooth}(\vec{x} + \vec{x}_0) - \vec{\alpha}_{halo}(\vec{x} + \vec{x}_0) = \int (\kappa_{smooth}(\vec{x} + \vec{x}_0) - \kappa_{halo}(\vec{x} + \vec{x}_0)) d\vec{x} \tag{57}$$

The approximation (55) and equation (57) give:

$$\vec{\alpha}_{smooth}(\vec{x} + \vec{x}_0) - \vec{\alpha}_{halo}(\vec{x} + \vec{x}_0) \approx f_\Sigma(\vec{x}_0) \kappa_{smooth}(\vec{x}_0) \vec{x} \tag{58}$$

If equation (58) is inserted into equation (56), the final lens equation for the simulation region is obtained:

$$\vec{y} = \vec{x} - \vec{\alpha}_{smooth}(\vec{x} + \vec{x}_0) + \vec{\alpha}_{smooth}(\vec{x}_0) + f_\Sigma \kappa_{smooth}(\vec{x}_0) \vec{x} - \vec{\alpha}_{sub}(\vec{x} + \vec{x}_0) \tag{59}$$

3.2 The grid setup

The simulation region is smaller than the projection of the halo upon the lens plane. Especially the image separation is larger than this region. Therefore, whenever the smooth model of the host halo predicts more than one image, these are treated separately. A square grid centered at $\vec{x}_0$ is used to approximate the simulation region and the length scale used is (29) with $\sigma = \sigma_{max}$ inserted. If the number of grid points along each side of the grid is N and the gridspacing is Δx, then the physical area of the simulation grid is: $\mathcal{A}_{grid} = ((N-1)\Delta x \xi_0(\sigma_{max}))^2$. The number of grid points and the length scale are kept fixed for a given mass range of substructure. The grid spacing is then used to adjust the area of the grid, so that it fits the subtructure configurations. In the simulations a 257^2 grid is used.

3.3 The substructure setup

3.3.1 The probability distribution

The subhalos are described by their mass distributions and coordinates in the lens plane. The truncated SIS used by Metcalf and Madau are described by the velocity dispersion σ and the distance to the center of the host halo R. The subclump radii and masses are functions of these two parameters and are given by equation (34). The number of satellites is supposed to be inversely proportional to the mass squared, $dN/dm \propto m^{-2}$. What is then the corresponding probability distribution? Since the mass of a subhalo is a function of σ, the probability distribution $P(\sigma)$ is needed rather than $P(m)$. The simulation region is small, which implies that the linear dependence on R of the subclump mass can be neglected. The satellite mass is proportional to the cube of the velocity dispersion, $m \propto \sigma^3$. This implies that $dm/d\sigma \propto \sigma^2$. The chain rule then gives:

$$\frac{dN}{d\sigma} = \frac{dN}{dm}\frac{dm}{d\sigma} \propto \frac{1}{\sigma^4} \tag{60}$$

If the velocity dispersion of the satellites is greater than σ_0 then the number of satellites with σ larger than this velocity dispersion should be:

$$N(>\sigma_0) \propto \int_{\sigma_0}^{\infty} \frac{dN}{d\sigma'} d\sigma' \propto \int_{\sigma_0}^{\infty} \frac{1}{\sigma'^4} d\sigma' = \frac{1}{\sigma_0^3} \tag{61}$$

In the same way the number of satellites with velocity dispersion larger than σ can be calculated:

$$N(>\sigma) \propto \frac{1}{\sigma^3} \tag{62}$$

The probability distribution for $\sigma > \sigma_0$ is thus:

$$P(\sigma > \sigma_0) = \frac{N(>\sigma)}{N(>\sigma_0)} = \left(\frac{\sigma_0}{\sigma}\right)^3 \tag{63}$$

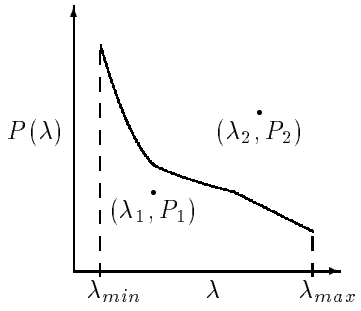

Figure 2: Generation of random numbers λ following a probability distribution $P(\lambda)$. The values of λ corresponding to points (λ, P) lying above (under) the probability curve is rejected (accepted).

3.3.2 The generation of random numbers

The random configuration of subclumps should obey the probability distribution (63) derived above. Random numbers λ that follow a probability distribution $P(\lambda)$ can be generated from two uniform random deviates [6]. These two uniform random deviates should have the following properties: $\lambda_{min} < \lambda < \lambda_{max}$ and $P(\lambda_{min}) < P < P(\lambda_{max})$. One can think of the two random numbers as a point in the plane spanned by λ and $P(\lambda)$, see figure 2. If the point lies under the probability curve, then the corresponding λ is accepted as a random number following the probability distribution. If the point lies above the curve, the corresponding λ is rejected. Thus the point (λ_1, P_1) in the figure corresponds to λ_1 while (λ_2, P_2) is rejected.

The program used to generate the uniform random deviates is written by C. Walck.

3.3.3 The total mass of the substructure

The total mass of the subhalos in the simulation region is a fraction of the mass of the host halo. If the surface density of the host halo in the simulation region can be approximated as constant, then the total mass of the host halo within this region M_{halo} is given by:

$$M_{halo} = \Sigma(\xi_0 \vec{x}_0) A_{grid} = \frac{\sigma_{halo}^2 (N-1)^2 \Delta x^2 \xi_0(\sigma_{max})}{2G|\vec{x}_0|} \tag{64}$$

where N is the number of grid points along each side of the grid and Δx is the grid spacing. The mass of the substructure within the simulation region is thus $M_{sub} = f_\Sigma M_{halo}$. Randomly distributed values of the parameter σ are generated by the method described in section (3.3.2). The upper and lower mass limits for the subhalos are described in terms of σ_{min} and σ_{max}. The coordinates of the subclumps are generated randomly with values limited by the size of the grid.

The number of subclumps is limited by M_{sub}. The algorithm used to create substructure is written so that substructure is created as long as the total mass of the subclumps does not exceed 90% of M_{sub}. The total mass of the substructure can therfore deviate from M_{sub}. For a large number of simulations these fluctuations should be evenly distributed so that they cancel out. If the total mass of the substructure is required to sum up exactly to M_{sub}, then there is a risk that the number of large subclumps is supressed.

3.4 The deflection angles caused by the substructure

3.4.1 Truncated SIS treated as point masses

When the deflection angles caused by the substructure are computed, the substructure is first treated as point masses. This approximation is justified by the fact that outside the truncation radius the deflection angle caused by a SIS is the same as the one caused by a point mass. The deflection angle can be obtained from the deflection potential. A quick way to find the potential of the point masses is to solve Poisson's equation (13) numerically. In order to do this both the source term $2\kappa(\vec{x})$ and the boundary conditions must be known. The exact boundary conditions can be calculated by superposition of the contribution from each subclump (50). The number of calculations needed to calculate the boundary conditon exactly is $\propto N_{clump}N_{grid}$, which is quite time–consuming if there is a large number of subclumps.

The point masses are moved to the closest grid point and the surface mass density is calculated by equation (48). A program written by R.C Le Bail, called ELPAHY, is used to solve Poisson's equation numerically. This partial differential equation solver utilizes fast fourier transforms and the finite difference method. The finite difference method can not deal with sharp edges or corners such as the delta–function. The delta–function must therefore be approximated in some way.

3.4.2 Approximation of the delta–function

A way of solving the problem mentioned in the previous section is to soften the peak. A two–dimensional Gaussian $G(\vec{x}) = \exp(-\beta\vec{x}^2)$ can be used to approximate the delta function. The slope of $G(\vec{x})$ can be made arbitrarily steep by varying the parameter β. The surface integral of the delta–function is by defintion unity, that is:

$$\int_{\mathcal{R}^2} \delta^2(\vec{x}) d^2x = 1 \tag{65}$$

Therefore the Gaussian must be normalized with its volume. On the grid the Gaussian is represented only by its value in a discrete number of points. It is convenient to rewrite the Gaussian so that the shape of it remains the same for different values of the gridspacing Δx. This can be done by a simple coordinate transformation, $\vec{x} \rightarrow \vec{x}/\Delta x$. The approximation of the delta–function to be used is thus:

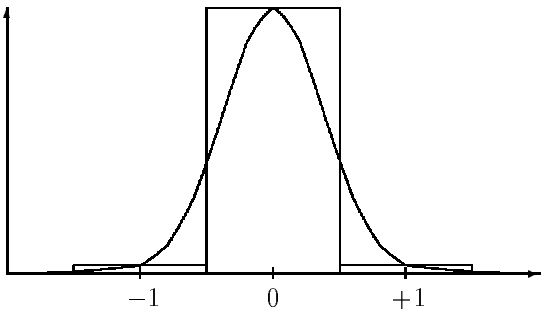

Figure 3: Representation of the delta function on a grid. The delta–function for fixed x_2 is depicted. The rectangles approximate the area of this representation.

$$\delta^2(\vec{x}) \approx \frac{1}{V\Delta x^2} e^{-\beta((x_1/\Delta x)^2+(x_2/\Delta x)^2)} \tag{66}$$

where V is the volume of the Gaussian on a grid with unity spacing. In figure 3 a picture of the Gaussian in one dimension is shown. The Gaussian is represented by values only at the points; $(-1, x_2)$, $(0, x_2)$ and $(+1, x_2)$. The area of this representation can be thought of as the rectangles shown in the figure. The corresponding volume can analogously be represented with boxes. The volume of the small boxes is $G(\vec{x})\mathcal{A}_{cell}$, where $\mathcal{A}_{cell} = 1$ is the area of a unity grid cell. An approximate value of V is thus obtained by simply adding the values of $G(\vec{x})$ at the grid points. The slope of the Gaussian is chosen to be $\beta = 3.5$. The volume on the unity grid, computed with the box approximation, is $V \approx 1.12$. This value of the volume of the Gaussian is larger than the value calculated analytically: $\int_{-\infty}^{\infty}\int_{-\infty}^{\infty} \exp(-\beta(x_1^2 + x_2^2))dx_1dx_2 = \pi/\beta = 0.898$. This discrepancy is due to the coarseness of the unity grid. How well this approximation of a pointlike mass works can be checked against the known solution $\psi(\vec{x}) = \frac{1}{2}\ln(x_1^2 + x_2^2)$. An even better agreement with the analytical solution can be achieved by using $V = 1.142$. The approximation of the delta–function represented as a matrix looks like (i.e. as the approximation looks like on the unity grid):

$$\begin{pmatrix} 0 & \cdots & 0 & 0 & 0 & 0 & 0 & \cdots & 0 \\ \vdots & \ddots & \vdots & \vdots & \vdots & \vdots & \vdots & \ddots & \vdots \\ 0 & \cdots & 0 & 0 & 0 & 0 & 0 & \cdots & 0 \\ 0 & \cdots & 0 & 0.001 & 0.03 & 0.001 & 0 & \cdots & 0 \\ 0 & \cdots & 0 & 0.03 & 1.0 & 0.03 & 0 & \cdots & 0 \\ 0 & \cdots & 0 & 0.001 & 0.03 & 0.001 & 0 & \cdots & 0 \\ 0 & \cdots & 0 & 0 & 0 & 0 & 0 & \cdots & 0 \\ \vdots & \ddots & \vdots & \vdots & \vdots & \vdots & \vdots & \ddots & \vdots \\ 0 & \cdots & 0 & 0 & 0 & 0 & 0 & \cdots & 0 \end{pmatrix} \tag{67}$$

3.4.3 Refined calculation of $\vec{\alpha}_{sub}(\vec{x})$

The point mass approximation does not hold inside the radius of a subhalo. Inside this radius the contribution to the deflection angle from the subhalo must be recalculated. The refined calculation will be carried out for a square patch larger than the area covered by the subhalo. The contribution to $\vec{\alpha}_{sub}(\vec{x})$ from the subhalo must first be subtracted from the points inside the square patch. The mass of a pointlike object will only affect the strength of the deflection potential and not its shape. This can be used to quickly find the contribution to the deflection angle from a specific point mass. If a point with unity mass, $\kappa(\vec{x}) = \pi\delta^2(\vec{x})$, is placed in the middle of a grid and its boundary values are exactly specified, then the numerical solution to the problem can be used to find the contribution from a point with arbritrary mass by just multiplying this solution with its surface mass density.

After the contribution from the point mass approximation has been removed from the square patch the exact contribution from that subclump is calculated by equation (45). The size of the square patch depends on the radius of the subclump under consideration. The formula used to calculate the number of grid points on the side of the square is $N_{patch} = 2N\left[\frac{r(\sigma,R)}{\xi_0(\sigma_{max})\Delta x} + 1\right] + 2N\left[5\frac{\sigma}{\sigma_{max}}\right]$, where by $N[\ldots]$ is meant the nearest integer. The first term makes sure that the square patch covers the area of the subclump. The second term scales the square path with the radius of the clump.

3.4.4 The outcome of the lensing equation

The lens mapping for the simulation region is given by equation (59). With this lens mapping the images for a given source can be reconstructed. The source position is calculated for every point in the grid and the grid points that lie within a specified source are recorded. The area of the image can then be estimated by the number of grid points corresponding to the source multiplied with the area of a grid cell. The magnification can then be calculated with equation (18). The algorithm is written so that it can handle images that do not lie entirely within the grid. If any of the grid points corresponding to an image lies on the boundary of the grid, the computation is redone for the

same substructure configuration but with a 10 % lager grid spacing Δx. This procedure goes on until the whole image is covered by the grid. The algorithm can thus handle multiple images at the expense of poorer resolution.

4 Results of the simulations

4.1 Lensing parameters

The smooth macro model is axially symmetric so that without loss of generality the source can be assumed to lie on the line $\vec{y} = (y, 0)$ in the lens plane. Consequently the images of the source will lie on the line $\vec{x} = (x, 0)$. If $0 < y < 1$ then the lens equation (31) for the SIS becomes $y = x \pm 1$. There will then be two images of the source. One image on opposite sides of the lens. In the case of $y > 1$ only one image will occur. This case is of no interest in this paper since it does not yield any flux ratios.

The source and lens are assumed to be located at redshift $z = 3$ and $z = 1$ respectively. A circular source with radius r is used. For all simulations the velocity dispersion of the macro lens is assumed to be 240 km s^{-1}. The value adopted for the Hubble constant is $H_0 = h \cdot 100$ km s^{-1} Mpc^{-1} with $h = 0.65$.

4.2 Different distributions of substructure

The distribution of substructure favoured by CDM simulations is $dN/dm \propto m^{-\beta}$ with $\beta = 2$. How much does the value of β influence the results of the simulations? In figure 4 the probability distributions of the magnifications for different values of β are plotted. In the upper left and right panels the distributions for the outer and inner images are depicted respectively. In the lower panel the distributions of difference in image brightness meassured in magnitudes are shown. The sets consisting of data for the outer and inner image are not correlated since they are treated separately. If for every point in the set of data for the outer image there is associated a point in the set of data for the inner image, it is nevertheless possible to obtain a probability distribution for the difference in image brightness. The difference in image brightness, meassured in magnitudes, for every pair of data is calculated by the following formula: $\Delta m = \ln(\mu_{outer}) - \ln(\mu_{inner})$.

The distribution of subhalos corresponding to different β can be derived with the same type of reasoning as used in section 3.3.1. The distributions in the figure were obtained for 500 simulations. 5% of the host halo mass was in subhalos of $10^4 M_\odot < m < 10^8 M_\odot$. The source coordinate and radius were $y = 0.12\ \xi_0(\sigma_{halo})$ and $r = 10$ pc respectively. The vertical dotted lines in the figure correpond to the results for a point source lensed in the absense of substructure.

The mass distribution can obviously have a large effect on the observable Δm. As can be seen from the lower panel a change in the exponent β by

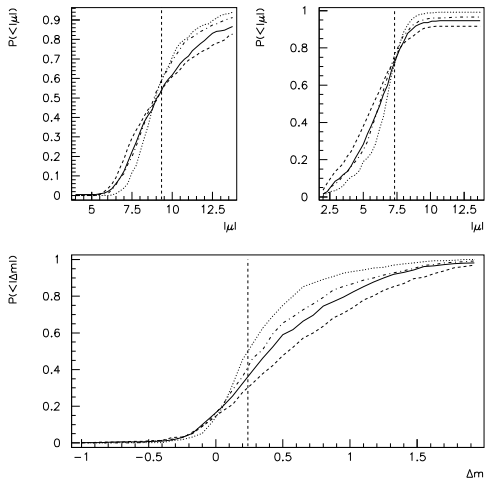

Figure 4: Probability distributions of magnifications for different mass distributions. In the left and right panels are the distributions for the outer and inner image depicted respectively. The cumulative difference in image brightness measured in magnitudes is shown in the lower panel. Negative values correspond to the cases when the inner image is brighter. The vertical dotted lines are the values for a point source lensed by the smooth macro lens in absense of substructure. The probability distributions in the figure correspond to $dN/dm \propto m^{-\beta}$. *Dashed curve:* $\beta = 1.8$. *Solid curve:* $\beta = 2$. *Dash-dotted curve:* $\beta = 2.1$. *Dotted curve:* $\beta = 2.3$.

more than ~ 10 % would give a rather different probability distribution for the difference in image brightness.

4.3 Image splitting

A circular source that is lensed by a singular isothermal sphere gives rise, under certain conditions, to two elliptical images on opposite sides of the lens. The presence of substructure can cause these images to be splitted once more. The most notable effect of this secondary splitting will occur for the larger subhalos since they affect the lensing more than the small ones. A typical situation in which the outer image is split in two is depicted in figure 5. This situation occured for a 10 pc source located at $y = 0.12\ \xi_0(\sigma_{halo})$ in the source plane. 5 % of the halo mass was in substructure of mass $10^4 M_\odot < m < 10^8 M_\odot$. In the figure there are two larger subhalos, with center of mass located nearly at the origin. If there were no substructure, the center of the image would be located at the origin. The two large subclumps act as a massive single lens, that splits the primary image into two secondary images. The distance in the lens plane between the two primary images is approximately 4500 pc , whereas the distance between the two secondary images is only approximately 150 pc. If $\Delta\xi$ is the separation of the images in the lens plane and D_d is the angular distance to the lens, the angular separation $\Delta\theta$ of the images is $\Delta\theta = \Delta\xi/D_d$. The lens is at

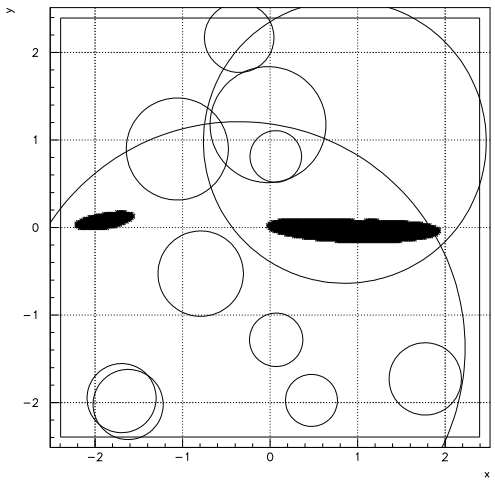

Figure 5: Image splitting caused by substructure. The solid circles mark the substructure. The size of the grid is indicated by the large solid square. The scale of the grid is $\xi_0(\sigma_{max}) \approx 54$ pc. In the absense of substructure the image of the circular source would be an ellips centered at $(0, 0)$. The image separation is approximatey 150 pc corresponding to an angular separation of $0.02''$.

redshift $z = 1$, which corresponds to $D_d = 1.4 \cdot 10^9$ pc. The angular separation of the primary and secondary images is thus $0.66''$ and $0.02''$ respectively. The separation of secondary images is thus only 3 % of the separation of the primary images.

It is plausible that only the largest subhalos cause secondary image splitting. This is beacuse smaller subhalos imply a larger number of subhalos, which in turn implies that the resulting potential is smoother than for a few large subhalos. If this is the case, then the separation of secondary images could be used to roughly estimate the mass of the subhalo responsible for the image splitting.

4.4 Comparison with Metcalf and Madau

Do the results of the simulations agree with the results of Metcalf and Madau? In figure 6 the cumulative distribution for different forms of substructure and different source sizes are plotted. The results of Metcalf and Madau for the same parameters are shown in figure 7. At first sight the results presented in the two figures do not seem to be consistent. But a closer look at the figures reveals that, the dependence on the fraction of substructure f_Σ is roughly the same in both figures. This can be seen by comparing the behaviour of curves corresponding to the same source size to each other. Thus the dependence of the fraction of substructure obtained here is roughly the same as the one Metcalf and Madau obtained. There is however one big difference beteween the curves

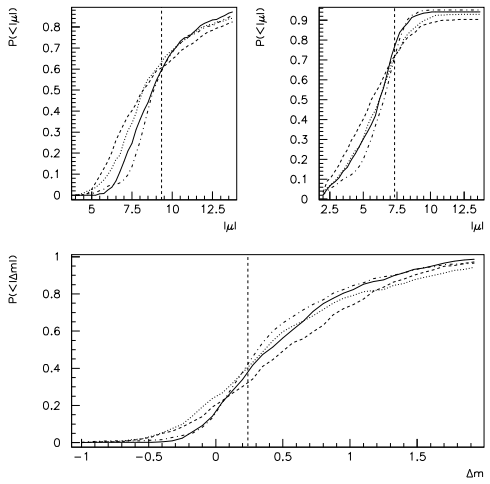

Figure 6: Cumulative probability distributions for different forms of substructure and source sizes. The *Solid curve* is the distribution obtained for $f_\Sigma = 5$ %, with subclump masses: $10^4 M_\odot < m < 10^8 M_\odot$ and a 10 pc source. The *Dash–dotted curve* is the same except that $f_\Sigma = 10$ %. The *Dashed curve* is the distribution obtained for $f_\Sigma = 5$ %, with subclump masses: $10^3 M_\odot < m < 10^7 M_\odot$ and a 1 pc source. The *Dotted curve* is the same except $f_\Sigma = 10$ % . The position of the sources was for all curves $y = 0.12\ \xi_0(\sigma_{halo})$.

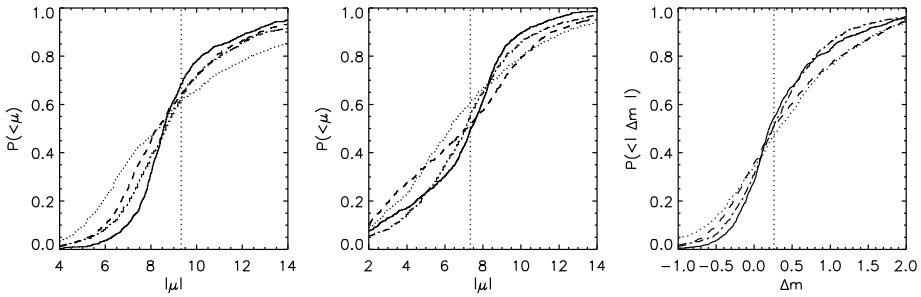

Figure 7: The results of Metcalf and Madau, figure 4 in reference [3]. The cumulative magnification distributions for the two images of a SIS lens with source position $y = 0.12$ measured in lensing scale lengths. The distribution of image 1 – the primary image or outer image – is plotted on the left. In the center is the distribution for image 2. On the right the cumulative distribution of the difference in image brightness measured in magnitudes is shown. Negative values of Δm correspond to the cases where image 2 is brighter than image 1. The vertical dotted lines are the values expected for a smooth lens and an infinitely small source. The different curves are for different forms of substructure and source sizes. The *solid curve* assumes that 5 % of the mass is in subslumps with $10^4 M_\odot < m < 10^8 M_\odot$, and a 10 pc source. *Dashed line:* The same except with 10% of the mass in substructure. *Dash–dotted curve:* assumes 5 % of the mass in subclumps with $10^3 M_\odot < m < 10^7 M_\odot$, and a 1 pc source. *Dotted curve:* same as the dash–dotted line only with 10 % of the mass in substructure.

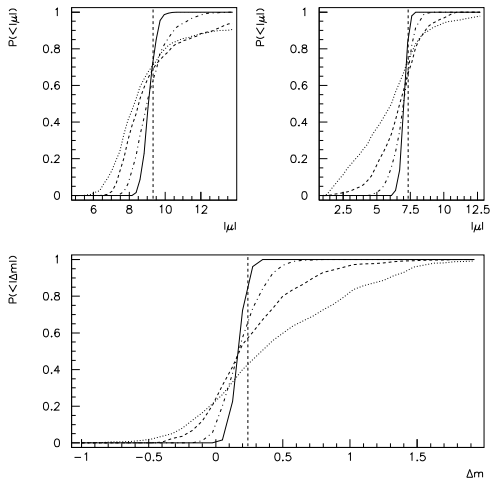

Figure 8: Cumulative probability distributions of magnification for different ranges of the mass m of the subhalos. *Solid curve:* $10^4 M_\odot < m < 10^5 M_\odot$. *Dash–dotted curve:* $10^5 M_\odot < m < 10^6 M_\odot$. *Dashed curve:* $10^6 M_\odot < m < 10^7 M_\odot$. *Dotted curve:* $10^7 M_\odot < m < 10^8 M_\odot$. The fraction of substructure is for all curves $f_\Sigma = 2$ %. The radius and position of the source are for all curves 10 pc and $y = 0.12\ \xi_0(\sigma_{halo})$ respectively.

obtained in this paper and in [3], namely the lack of low magnifications in the former. The absence of low magnification can be explained by the resolution problem that will be discussed in section 4.5.2. This effect is systematic so that the probability distributions for the observable difference in image brightness are almost the same.

In figure 8 the probability distributions for different ranges of masses of substructure are plotted. In figure 9 the corresponding results of Metcalf and Madau are shown for comparison. The relations beween the different curves presented in this paper are essentially the same as the relations between the curves of Metcalf and Madau. However the distributions for the largest subclumps $10^7 M_\odot < m < 10^8 M_\odot$ are not at all alike. For some values of the magnification the curves in [3] are vertical. This implies that the probability of that value of the magnification is high. This might be an effect that arises when the contribution from many large subclumps are considered. The algorithm used here can not handle many large subclumps with good resolution of the images. So that the probability curves for subclumps with mass $10^7 M_\odot < m < 10^8 M_\odot$ is obtained with only one or a few subhalos.

4.5 Reliability of the method

This section contains a discussion of the reliability of the results of the simulations and the sensitivity of the results to the simulation parameters.

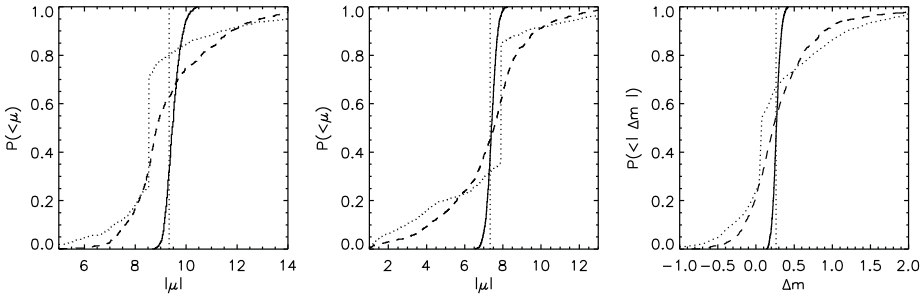

Figure 9: The results of Metcalf and Madau, figure 6 in reference [3]. The cumulative magnification distribution for the two images of a 10 pc source with source position $y = 0.12$. The three different curves correspond to different subclump mass ranges. *Solid line:* $10^4 M_\odot < m < 10^5 M_\odot$. *Dashed line:* $10^6 M_\odot < m < 10^7 M_\odot$. *Dotted line:* $10^7 M_\odot < m < 10^8 M_\odot$. The mass fraction in subclumps, f_Σ, is held fixed at 2 %. The subclumps are progressively more influential as they get more massive despite their smaller number density. The vertical sections of the dotted curves are located at the background magnifications – the value of the magnification when there are no subclumps influencing the image.

4.5.1 Image resolution

How reliable is the method used to compute the magnification of the source? The magnification is given by the ratio of the image and source areas. The number of grid points N found to correspond to a given source and the area of the grid cells are used to calculate the area of the image. If the number of grid points N increases, the error in the calculation of the area should decrease. In practice the total number of gridpoints is held fixed, so that a higher resolution of the images is obtained by shrinking the area of the grid cells. When counting the number of gridpoints corresponding to images the error is expected to be $\sim \sqrt{N}$. The relative error in N is thus, $\Delta N \sim \sqrt{N}/N = N^{-1/2}$. In figure 10 the relative error for the magnification of the outer image of a SIS is plotted versus N. The relative error was computed under the assumption that the true magnification is the same as for a point source μ_{point}. The relative error is then $\Delta\mu = \mu/\mu_{point} - 1$. As can be seen from figure 10 the relative errors in the magnification are somewhat lower than expected, but follows the curve nicely. This is due to the fact that the source is extended. The magnification of an extended source μ_e is smaller than the magnification of a point source. This implies that $\mu/\mu_e > \mu/\mu_{point}$ and $(\Delta\mu)_e > (\Delta\mu)_{point}$. The points in the figure therefore represent a lower limit of the relative error. From the distribution $N^{-1/2}$ it can be seen that ~ 400 points is sufficient to compute the magnification with an accuracy of ~ 5 %. The grid spacing Δx must thus be carefully chosen so that N is large enough even for small magnifications, i.e. relatively small images.

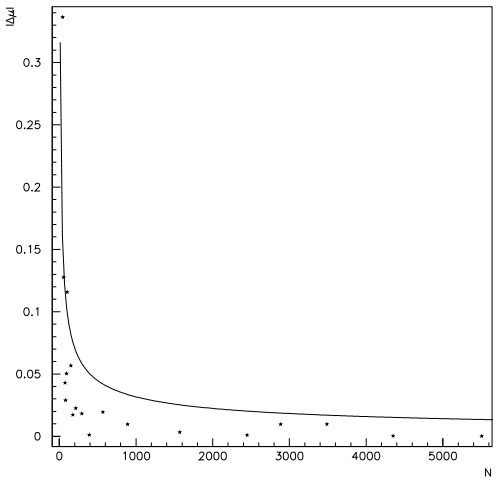

Figure 10: The figure shows the relative errors $|\Delta\mu|$ in the magnification versus the number of points N used to compute the area of the image. The solid curve is $\Delta N = N^{-1/2}$. The relative error in the magnification is calculated with respect to the magnification of a point source, $\Delta\mu = \mu/\mu_{point} - 1$. From the figure it is evident that the relative errors follow the distribution $N^{-1/2}$.

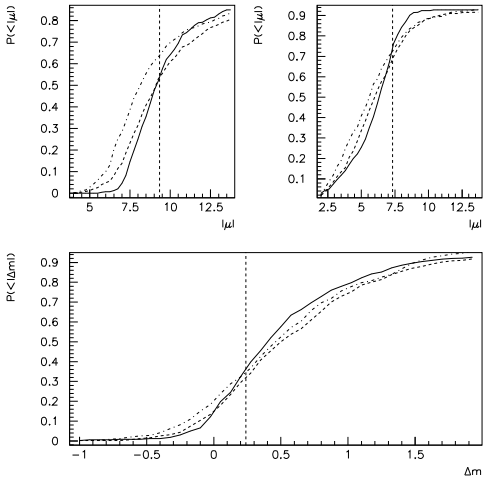

Figure 11: The influence of grid spacing Δx on the probability distributions of magnifiacations. The distributions were obtained for; $f_\Sigma = 10$ %, $y = 0.12\ \xi_0(\sigma_{halo})$, $r = 10$ pc and the mass range were $10^3 M_\odot < m < 10^7 M_\odot$. The upper left and right panels show the cumulative distributions for the outer and inner image respectively. In the lower panel the cumulative distributions for the difference of image brightness measured in magnitudes are shown. *Solid curve:* $\Delta x = 0.005$ corresponding to $\sim$ 10 subclumps . *Dashed curve:* $\Delta x = 0.01$ corresponding to $\sim$ 20 subclumps. *Dash−dotted curve:* $\Delta x = 0.02$ corresponding to $\sim$ 30 subclumps.

4.5.2 The size of the grid

In section 4.5.1 the resolution of individual images was discussed. The question in this section is how the size of the grid (i.e. the resolution) affect the statistics of a large number of simulations? If all lensing parameters but the grid spacing Δx is kept fixed how will it affect the probability distributions? A larger value of the grid spacing Δx implies a larger grid, which contains more mass and more substructure. In figure 11 the cumulative probability distributions for different values of Δx are shown. In the upper left and right panels the distributions for the outer and inner image are plotted respectively. In the lower panel the cumulative distribution of the difference in image brightness of the different images measured in magnitudes is plotted. As can be seen from the figure, the grid spacing do affect the result. The larger the grid spacing is, the larger is the spread in the distribution. For small values of the grid spacing the probability for small and large magnifications is suppressed. The most important thing to note here is that an increasing number of subhalos implies an increasing probability of small magnifications. This might be an explanation of the lack of small magnifications for the largest subhalos found in section 4.4.

Why is the probability distributions of magnifications affected by the size of the grid? If the grid is to small, then the substructure just outside the grid can not be approximated with a smooth potential. The grid must be so large that the contribution to the lensing potential from any substructure outside the grid can be treated as a part of the smooth host halo. For subclumps that are small compared with the image this should not be a problem. If the subclumps are large compared to the image, then the need for a sufficiently large grid will be in conflict with the need for good resolution. If the grid is small and the subclumps are large, then the grid can only contain one or a few subclumps. The method used for generation of substructure does not allow for the possibility that the grid may be under– or over dense compared to the average distribution of subclumps. If the simulation region can be under– or over dense, then the spread in the distribution of magnifications should be larger. Another possibility that arises when the number of subclumps rises is that the contributions to the deflection potential from each subclump may to some extent cancel out. The distributions should then tend to the smooth case.

4.5.3 Statistics

If several simulations are made for the same simulation parameters, then it is possible to obtain probability distributions for the magnification in the presence of substructure. A question that naturally arises is, how many simulations are needed to obtain good statistics? In figure 12 the cumulative magnification distributions obtained for 500, 1000 and 5000 simulations are compared to the distribution obtained for 10000 simulations. In the upper left panel the distribution obtained for 500 and 10000 simulations are drawn. With the data from 500 simulations it is possible to recover the charateristic shape of the probability distribution. As can be seen from the upper right panel the distrubution

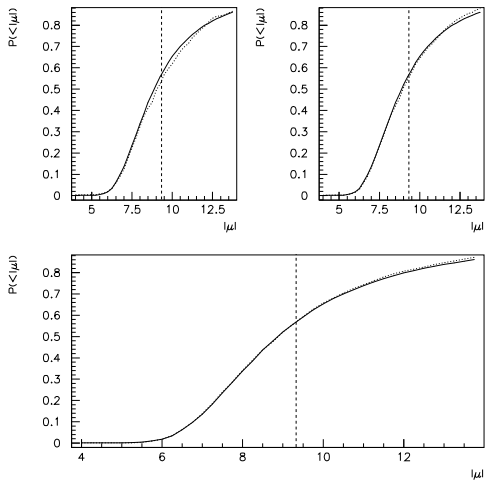

Figure 12: Comparison of the magnification distributions for different number of simulations. The solid line corresponds to the magnifaction distribution obtained for 10000 simulations. The dotted line in the upper left and right panels corresponds to the distribution obtained for 500 and 1000 simulations respectively. In the lower panel the distribution for 5000 simulations is plotted as a dotted line. The vertical dashed line in the figures shows the magnification for a point source lensed by a SIS. 500 simulations seem to be enough to get a rough estimate of the probability distribution. The distributions based on more than 1000 simulations deviates only a little from each other.

obtained for 1000 simulations is quite good. In the lower panel the distribution for 5000 and 10000 simulations are plotted. The agreement betweeen these two curves is execellent. From the above discussion it is clear that ~ 500 simulations can be used to get a quick estimation of the probability distributions. If a more accurate distribution is neded more than 1000 simulations are necessary.

5 Conclusions

In the above it has been shown that a small change in the distribution of subhalos would give a significant change in the probability distributions of magnifications.

The simulations have also shown that substructure can cause secondary splitting of the images. The expected separation of the secondary images is of the order of 10 milli–arcseconds. If the splitting can be observed it could be used to estimate the mass of the substructure.

The results presented in this paper are consistent with the results of Metcalf and Madau except for the largest subhalos. The discrepancies between the probability distributions of magnifications can probably be explained by the fact that the method presented here is not capable of dealing with large subclumps.

There are two solutions to the problem of simulating gravitational lensing with large subhalos. The first one is to increase the number of grid points. This

has the advantage that it will give very good estimates of the magnification for each simulation and it allows much more substructure. The obvious disadvantage is of course that the simulations will take longer time to perform. The other approach is to distribute the substructure over a grid that is larger than the one that is actually used. The larger grid could obviously contain more substructure than the small one. The mean density of substructure should be the same on the smaller grid, but there is also the possibility that the smaller grid is denser than it is on average. In that case it contains more substructure, which is good. This approach should reflect a more realistic model, then the one used in this paper. For small subclumps there is no difference, but for the large ones there should be a difference between the two models. Keeping track of more substructure than necessary might be a burden for the computer, why it should be used only when necessary.

It would also be interesting to use more realistic models for the macro model and the substructure. The approximation with point masses can be done outside all truncated spherically symmetric mass distributions, so the basic ideas of the method can still be used.

References

[1] Mao S., Schneider P. *1998 MNRAS, 295, 587*

[2] Moore B. *2001 The dark matter crisis,* (astro-ph/0103100)

[3] Metcalf R.B., Madau P. *2001 ApJ in press,* (astro-ph/0108224)

[4] Schneider P., Ehlers J., Falco E.E. *1992 Gravitational Lenses,* (Springer–Verlag Berlin)

[5] Narayan R., Bartelmann, M. *2001 Lectures on Gravitational Lensing,* (astro-ph/9606001)

[6] Press W.H., Teukolsky S.A., Vetterling W.T., Flannery B.P. *1994 Numerical recipes in Fortran, second edition* (Cambridge university press)

[7] Ekman T., Eriksson G. *1984 Programmering i Fortran 77,* (Studentlitteratur)